J|A|C|S ARTICLES

Published on Web 03/11/2010

Metallization of a Hypervalent Radical Dimer: Molecular and Band Perspectives

John S. Tse,[†] Alicea A. Leitch,[‡] Xueyang Yu,[§] Xuezhao Bao,[§] Sijia Zhang,[||] Qingqing Liu,[||] Changqing Jin,[||] Richard A. Secco,[§] Serge Desgreniers,[⊥] Yasuo Ohishi,[#] and Richard T. Oakley*[,‡]

Department of Physics and Engineering Physics, University of Saskatchewan, Saskatoon, Saskatchewan S7N 5E2, Canada, Department of Chemistry, University of Waterloo, Waterloo, Ontario N2L 3G1, Canada, Department of Earth Sciences, University of Western Ontario, London, Ontario N6A 5B7, Canada, Institute of Physics, Chinese Academy of Sciences, Beijing 100080, China, Department of Physics, University of Ottawa, Ottawa, Ontario K1N 6N5, Canada, and Materials Science Division, Japan Synchrotron Radiation Research Institute (JASRI), SPring-8, Sayo, Hyogo 679-5198, Japan

Received January 10, 2010; E-mail: oakley@uwaterloo.ca

Abstract: Variable pressure and temperature conductivity measurements on the bisthiaselenazolyl radical dimer [**1a**]$_2$ have established the presence of a weakly metallic state over the pressure range 5−9 GPa. To explore the origin of this metallization we have examined the crystal and molecular structure of [**1a**]$_2$ as a function of pressure. At ambient pressure the dimer consists of two radicals linked by a hypervalent 4-center 6-electron S···Se−Se···S σ-bond into an essentially coplanar arrangement. The dimers are packed in cross-braced slipped π-stack arrays running along the *x*-direction of the monoclinic (space group $P2_1/c$) unit cell. Pressurization to 4 GPa induces little change in the molecular structure of [**1a**]$_2$ or in the slipped π-stack crystal architecture. Near 5 GPa, however, stress on the dimer leads to buckling of the two halves of the molecule and a contraction in the metrics of the S···Se−Se···S unit. These structural changes can be understood in terms of an electronic configurational switch from a 4-center 6-electron σ-bonded dimer to a more conventional π-bonded arrangement. At the same time the slipped π-stack arrays undergo a concertina-like compression, and the crystal structure experiences highly anisotropic changes in cell dimensions. DFT calculations on the molecular electronic structure of the dimer indicate a marked decrease in the HOMO−LUMO gap as the dimer buckles. Related solid-state calculations indicate a rapid closure of the valence/conduction band gap in the same pressure region and the formation of a quasi-metallic state. Metallization of [**1a**]$_2$ thus arises as much from intramolecular changes, which give rise to a collapse of the HOMO−LUMO gap and near coalescence of the valence and conduction bands, as from increased intermolecular interactions, which cause widening and overlap of the band edges.

Introduction

The use of pressure to modify the crystal structure and electronic properties of materials has a long history.[1] The current challenge in this area is largely focused on the very high compression regime, that is, the 200−300 GPa range.[2] However, even relatively low pressures (below 20 GPa) can have a significant effect on the electronic properties of molecular compounds, although full metallization of single component, closed shell organic materials has only rarely been observed, typically in condensed ring aromatics. For example, the activation energy, E_{act}, of single crystals of pentacene can be reduced to zero near 27 GPa, although for powdered samples higher pressures are required.[3] Metallization has also been observed in iodine-substituted aromatics, for example, *p*-diiodobenzene,[4] hexaiodobenzene,[5] and iodonil,[6] but the onset of the metallic state for these systems typically requires pressures in excess of 30 GPa. The possibility of band gap closure has been suggested as the source of metallization for these systems, but bond

[†] University of Saskatchewan.
[‡] University of Waterloo.
[§] University of Western Ontario.
[||] Chinese Academy of Sciences.
[⊥] University of Ottawa.
[#] Japan Synchrotron Radiation Research Institute.

(1) (a) Grochala, W.; Hoffmann, R.; Feng, J.; Ashcroft, N. W. *Angew. Chem., Int. Ed.* **2007**, *46*, 3620. (b) MacMillan, P. F. *Chem. Soc. Rev.* **2006**, *35*, 855.
(2) (a) Eremets, M. I.; Trojan, I. A.; Medvedev, S. A.; Tse, J. S.; Yao, S. *Science* **2008**, *319*, 1506. (b) Goncharenko, I.; Eremets, M. I.; Hanfland, M.; Tse, J. S.; Amboage, M.; Yao, Y.; Trojan, I. A. *Phys. Rev. Lett.* **2008**, *100*, 045504.
(3) Aust, R. B.; Bentley, W. H.; Drickamer, H. G. *J. Chem. Phys.* **1964**, *41*, 1856.
(4) Brillante, A.; Della Valle, R. G.; Farina, L.; Venutti, E.; Cavazzoni, C.; Emerson, A. P. J.; Syassen, K. *J. Am. Chem. Soc.* **2005**, *127*, 3038.
(5) (a) Nakayama, A.; Aoki, K.; Carlòn, R. P. *Phys. Rev. B: Condens. Matter* **2001**, *64*, 064104. (b) Nakayama, A.; Fujihisa, H.; Takemura, K.; Aoki, K.; Carlòn, R. P. *Synth. Met.* **2001**, *120*, 767. (c) Iwasaki, E.; Shimizu, K.; Amaya, K.; Nakayama, A.; Aoki, K.; Carlòn, R. P. *Synth. Met.* **2001**, *120*, 1003.
(6) (a) Nakayama, A.; Fujihisa, H.; Aoki, K.; Shirotani, I. *Synth. Met.* **1999**, *103*, 1901. (b) Nakayama, A.; Aoki, K.; Matsushita, Y.; Shirotani, I. *Solid State Commun.* **1999**, *110*, 627. (c) Shirotani, I.; Hayashi, J.; Yakushi, K.; Takeda, K.; Yokota, T.; Shimizu, K.; Amaya, K.; Nakayama, A.; Aoki, K. *Phys. B* **2001**, *304*, 6.

 10.1021/ja100216c

Chart 1

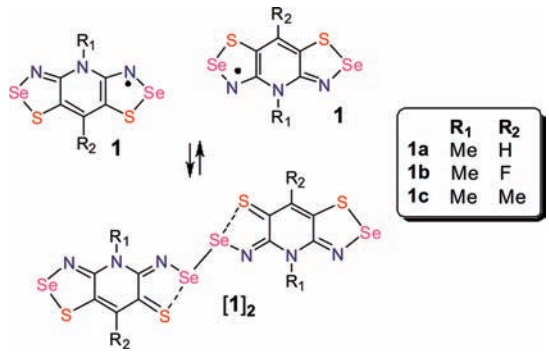

dissociation to afford domains of metallic iodine has also been implicated.[7] Compression has also been shown to enhance the conductivity of sulfur-,[8] selenium-,[9] and tellurium-based[10] heterocycles, but metallic or metal-like behavior requires pressures approaching or in excess of 20 GPa. However, for the elemental chalcogens, it is well-known that bond dissociation and structural rearrangements can occur under pressure.[11] In the case of sulfur, for example, increasing compression from 0−11 GPa at elevated temperature leads to opening of the S_8 rings of the orthorhombic phase to produce a helical chain (trigonal) structure, which in turn recyclizes to a rhombohedral structure based on S_6 rings.[12] Analogous trigonal[13] and rhombohedral[14] phases are also known for selenium.

In the light of these results, the behavior of the bisthiaselenazolyl radical dimer [**1a**]$_2$ (Chart 1, R_1 = Me, R_2 = H) is noteworthy. We first reported this compound in 2005,[15] as part of ongoing efforts to generate conductive and magnetic materials using heavy atom (selenium-based) radicals.[16] Since then we have successfully prepared, by judicious choice of R_1/R_2 groups, a wide variety of undimerized materials using radicals based on the framework of **1**, and many of these show interesting conductive and magnetic properties. Even though the spins in [**1a**]$_2$ were quenched by dimerization, its transport properties were nonetheless of interest. While its behavior at ambient pressure was normal, that is, it was a diamagnetic, small band gap semiconductor with a room temperature conductivity σ(300 K) of 2.3×10^{-6} S cm^{-1} and thermal activation energy E_{act} of 0.32 eV, what made this material remarkable was the dependence of its conductivity on pressure. Initial measurements using a cubic anvil press indicated that upon compression to 5 GPa, the value of σ(300 K) of [**1a**]$_2$ increased by 5−6 orders of magnitude, and E_{act} dropped to a plateau value near 0.03 eV.

The unanswered question at the time was the cause of this dramatic response, that is, the quasi-metallization of a molecular compound at only 5 GPa. Was it the result of molecular decomposition or the closure of an electronic band gap? With respect to the first possibility, neither sulfur nor selenium, two of the most likely potential degradation products, display appreciable conductivities under these pressure conditions.[17,18] More importantly, however, post-pressurization infrared measurements showed no sign of sample decomposition. To explore the second possibility, that the enhancement in conductivity was a feature of the crystal and hence solid-state electronic structure of the dimer, we prepared and structurally characterized the *isostructural* dimers [**1b**]$_2$ (R = F) and [**1c**]$_2$ (R = Me). The latter two materials showed a similar, although slightly less dramatic, pressure response,[19] on the basis of which we concluded that the source of the increase in conductivity for all three dimers was their common crystal and molecular structure. In an attempt to establish the nature of the structural changes that occur with compression and hence the origin of the enhancement in conductivity, we have carried out a detailed investigation of the crystal structure of [**1a**]$_2$ over the pressure range 0−10 GPa, using synchrotron radiation and diamond anvil cell techniques. Herein we describe the results of these crystallographic studies, which reveal changes in both the crystal and molecular structure of the dimer with increasing pressure that are consistent with a first-order phase transition between 4−5 GPa. Additional conductivity measurements as a function of pressure have also been undertaken, and these confirm the existence of a weakly metallic state at pressures above 5 GPa. The experimental results are interpreted in the light of density functional theory (DFT) calculations of the crystal and molecular electronic structure of the dimer as a function of pressure. While closure of the electronic band gap during the phase transition may be attributed in part to a broadening of the valence and conduction bands of the crystal structure, a more important factor is the internal electronic reorganization of the dimer itself, a process that gives rise to a sharp decrease in the HOMO−LUMO gap.

Results

Crystallography. High-pressure diffraction data on [**1a**]$_2$ were collected at room temperature as a function of increasing pressure using synchrotron radiation (λ = 0.51446 Å) and a diamond anvil cell with helium as the pressure transmitting

(7) Tateyama, Y.; Ohno, T. *J. Phys.: Condens. Matter* **2002**, *14*, 10429.
(8) Cui, H.; Brooks, J. S.; Kobayashi, A.; Kobayashi, H. *J. Am. Chem. Soc.* **2009**, *131*, 6358.
(9) (a) Shirotani, I.; Kamura, Y.; Inokuchi, H.; Hirooka, T. *Chem. Phys. Lett.* **1976**, *40*, 257. (b) Onodera, A.; Shirotani, I.; Inokuchi, H.; Kawai, N. *Chem. Phys. Lett.* **1974**, *25*, 296.
(10) Cui, H.; Okano, Y.; Zhou, B.; Kobayashi, A.; Kobayashi, H. *J. Am. Chem. Soc.* **2008**, *130*, 3738.
(11) (a) Akahama, Y.; Kobayashi, M.; Kawamura, H. *Phys. Rev. B* **1993**, *48*, 6862. (b) Luo, H.; Greene, R. G.; Ruoff, A. L. *Phys. Rev. Lett.* **1993**, *71*, 2943. (c) Akahama, Y.; Kobayashi, M.; Kawamura, H. *Phys. Rev. B* **1993**, *47*, 20.
(12) Crapanzano, L.; Crichton, W. A.; Monaco, G.; Bellissent, R.; Meouar, M. *Nat. Mater.* **2005**, *4*, 550.
(13) Cherin, P.; Unger, P. *Inorg. Chem.* **1967**, *6*, 1589.
(14) Miyamoto, Y. *Jpn. J. Appl. Phys.* **1980**, *19*, 1813.
(15) Beer, L.; Brusso, J. L.; Haddon, R. C.; Itkis, M. E.; Kleinke, H.; Leitch, A. A.; Oakley, R. T.; Reed, R. W.; Richardson, J. F.; Secco, R. A.; Yu, X. *J. Am. Chem. Soc.* **2005**, *127*, 1815.
(16) (a) Leitch, A. A.; Brusso, J. L.; Cvrkalj, K.; Reed, R. W.; Robertson, C. M.; Dube, P. A.; Oakley, R. T. *Chem. Commun.* **2007**, 3368. (b) Robertson, C. M.; Myles, D. J. T.; Leitch, A. A.; Reed, R. W.; Dooley, D. M.; Frank, N. L.; Dube, P. A.; Thompson, L. K.; Oakley, R. T. *J. Am. Chem. Soc.* **2007**, *129*, 12688. (c) Robertson, C. M.; Leitch, A. A.; Cvrkalj, K.; Reed, R. W.; Myles, D. J. T.; Dube, P. A.; Oakley, R. T. *J. Am. Chem. Soc.* **2008**, *130*, 8414. (d) Robertson, C. M.; Leitch, A. A.; Cvrkalj, K.; Myles, D. J. T.; Reed, R. W.; Dube, P. A.; Oakley, R. T. *J. Am. Chem. Soc.* **2008**, *130*, 14791. (e) Leitch, A. A.; Yu, X.; Winter, S. M.; Secco, R. A.; Dube, P. A.; Oakley, R. T. *J. Am. Chem. Soc.* **2009**, *131*, 7112.
(17) Selenium enters a metallic phase near 25 GPa. See: (a) Riggleman, B. M.; Drickamer, H. G. *J. Chem. Phys.* **1962**, *37*, 446. (b) Bundy, F. P.; Dunn, K. J. *J. Chem. Phys.* **1979**, *71*, 1550.
(18) Sulfur is converted into a metallic state at pressures above 40 GPa. See: (a) Chhabildas, L. C.; Ruoff, A. L. *J. Chem. Phys.* **1977**, *66*, 983. (b) Dunn, K. J.; Bundy, F. P. *J. Chem. Phys.* **1977**, *67*, 5048. (c) Peanasky, M. J.; Jurgenen, C. W.; Drickamer, H. G. *J. Chem. Phys.* **1984**, *81*, 6407.
(19) Leitch, A. A.; Yu, X.; Robertson, C. M.; Secco, R. A.; Tse, J. S.; Oakley, R. T. *Inorg. Chem.* **2009**, *48*, 9874.

Table 1. Crystal Data[a] of [**1a**]$_2$ as a Function of Pressure

	Pressure, GPa					
	0[b]	1.86	2.76	3.74	5.09	9.37
a, Å	4.924(4)	4.83377(8)	4.60771(12)	4.57430(14)	3.94301(9)	3.73682(19)
b, Å	12.616(11)	12.57757(18)	12.69423(20)	12.67862(24)	14.08054(31)	14.0175(6)
c, Å	15.086(13)	14.80061(30)	14.0065(4)	13.8297(4)	13.2227(4)	12.7420(9)
β, deg	94.563(14)	93.2827(16)	89.3851(20)	88.6518(26)	85.5588(28)	87.144(6)
V, Å^3	934.1(14)	898.36(3)	819.21(3)	801.84(4)	731.91(3)	666.61(6)
space group	$P2_1/c$	$P2_1/c$	$P2_1/c$	$P2_1/c$	$P2_1/c$	$P2_1/c$
Z	2	2	2	2	2	2
temp, K	295(2)	293(2)	293(2)	293(2)	293(2)	293(2)
λ, Å	0.71073	0.51446	0.51446	0.51446	0.51446	0.51446
solution method	direct methods	powder data	powder data	powder data	powder data	powder data
R_p	0.0439[c]	0.0056	0.0069	0.0076	0.0081	0.0091
R_{wp}	0.0939[c]	0.0098	0.0119	0.0126	0.0128	0.0135

[a] The unconventional cell settings (with $\beta < 90°$) at higher pressure were used so as to allow a direct comparison across all the structures. [b] Single crystal X-ray diffraction data from ref 15. [c] *R*, R_w for single crystal data.

Table 2. Selected Distances[a] and Angles[b] in [**1a**]$_2$ as a Function of Pressure

	Pressure, GPa					
	0[c]	1.86	2.76	3.74	5.09	9.37
Se2−Se2′	2.460(2)	2.490	2.476	2.490	2.724	2.669
Se2···S2	2.785(3)	2.708	2.685	2.678	2.252	2.190
S2−C4	1.694(6)	1.761	1.751	1.750	1.767	1.808
δ_1	0.384	0.279	0.079	0.156	1.578	1.655
δ_2	3.540	3.520	3.379	3.302	3.119	2.997
τ	46.0	46.7	47.2	46.2	52.3	53.3
ϕ	167.8	166.9	166.9	165.1	145.6	140.8
Se2···S1′, d_1	3.663	3.424	3.197	3.173	3.077	2.890
S2···Se1′, d_2	3.824	3.745	3.490	3.495	3.856	3.589
Se2···S1′, d_3	4.848	4.815	4.588	4.570	3.579	3.444
S2···Se1′, d_4	3.177	3.096	2.935	2.896	2.843	2.723

[a] Distances in angstroms. [b] Angles in degrees. [c] Data from ref 15.

medium. A total of five data sets up to 9.37 GPa were indexed,[20] and the structures were solved starting from a model radical **1a** derived from a fully optimized UB3LYP/6-311G(d,p) calculation. During the initial Rietveld refinement, performed using DASH, a rigid-body constraint was maintained, but the sulfur and selenium positions were later released to optimize within the plane of the molecule. Final refinement, using fixed atomic positions and isotropic thermal parameters, was performed using GSAS. Unit cell and refinement parameters are listed in Table 1, while summaries of pertinent inter- and intramolecular distances as a function of pressure are presented in Table 2. Figure 1 provides the atom numbering scheme and also defines some important intermolecular distances and angles.

At the molecular level and at ambient pressure, the crystal structure of [**1a**]$_2$ consists of pairs of radicals linked laterally into dimers across an inversion center by a hypervalent S2···Se2−Se2′···S2′ diselenide bond. This nearly linear 4-atom unit locks the two radicals into an almost coplanar arrangement, as indicated by the small value for δ_1, the mutual displacement of the mean molecular planes of the two halves of the dimer (Figure 1). With the formation of the diselenide the two Se2−S2 bonds open to a distance intermediate between the sum of the covalent radii[21] and the expected van der Waals contact.[22] At the same time the C4−S2 distances shorten, in accord with the valence bond representation provided in Chart 1. Whether the terminal C═S linkages are best referred to as full double bonds is not clear, as aromatic thiones (unless complexed to a metal) are uncommon.[23] Nonetheless, the C4−S2 distances in [**1a**]$_2$

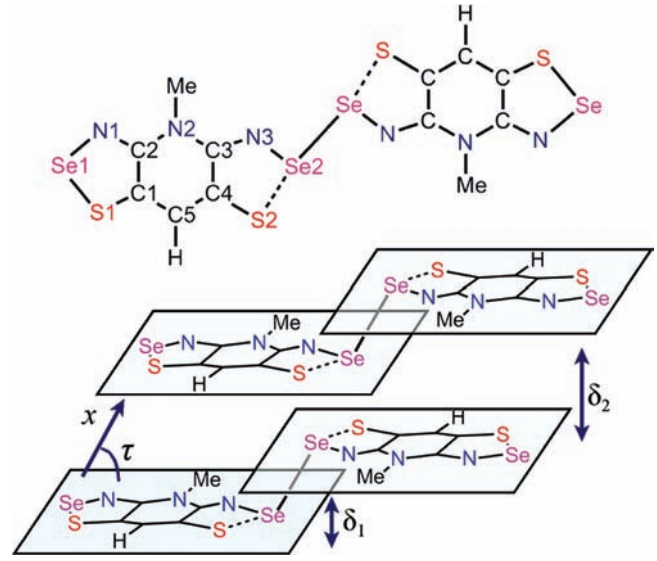

Figure 1. Atom numbering scheme and intermolecular structural parameters.

(20) The space group settings were adjusted so as to allow a direct comparison of all the high pressure cell parameters with those published for the ambient pressure crystal structure.
(21) Chen, C. M.; Dojahn, J. G.; Wentworth, W. E. *J. Phys. Chem. A* **1997**, *101*, 3088.
(22) (a) Bondi, A. *J. Phys. Chem.* **1964**, *68*, 441. (b) Dance, I. *New J. Chem.* **2003**, *27*, 22.
(23) (a) Moussa, J.; Lev, D. A.; Boubekeur, K.; Rager, M. N.; Amouri, H. *Angew. Chem., Int. Ed.* **2006**, *45*, 3854. (b) Cordes, A. W.; Koenig, H.; Oakley, R. T. *Acta Crystallogr.* **1987**, *C43*, 2468.

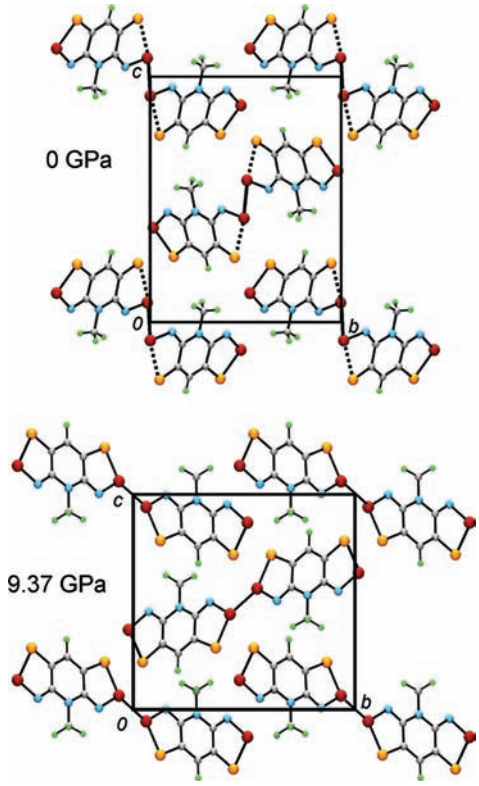

Figure 2. Unit cell of $[\mathbf{1a}]_2$, viewed down the stacking direction, at 0 and 9.37 GPa.

are comparable to those found in thioureas.[24] While this lateral mode of dimerization for a π-radical is rare,[25,26] hypervalent 4-center 6-electron (4c-6e)[27] dichalogenides RE−ER (E = S, Se, Te) stabilized on either side by coordination from lone pairs on *saturated* centers are relatively common.[28] Homonuclear dissociation of these latter species into radicals has not, however, been observed, presumably because spin density on the resulting radical would be largely localized on the chalcogen. By contrast, in π-radicals such as **1**, where spin density is delocalized across the entire heterocyclic framework, dissociation is more favorable. Nonetheless, for a model dimer $[\mathbf{1}]_2$ with $R_1 = R_2 = H$, DFT calculations (B3LYP/6-31G(d,p)) indicate a gas-phase bond dissociation enthalpy ΔH_{diss} of 18.2 kcal mol^{-1}.[15] In this light, it is quite remarkable that so many undimerized radicals based on this framework have been characterized.

The ambient pressure crystal structure of $[\mathbf{1a}]_2$ belongs to the monoclinic space group $P2_1/c$ and consists of ribbonlike arrays of radical dimers packed into interpenetrating, cross-braced π-stacks. A unit cell diagram, viewed down the stacking direction (the *x*-axis), is illustrated in Figure 2. The high pressure crystallographic data reveal that the same description can be applied, at least qualitatively, to the crystal structure of $[\mathbf{1a}]_2$

(24) Venkatachalam, T. K.; Sudbeck, E.; Uckun, F. M. *J. Mol. Struct.* **2005**, *751*, 41.
(25) Leitch, A. A.; McKenzie, C. E.; Oakley, R. T.; Reed, R. W.; Richardson, J. F.; Sawyer, L. D. *Chem. Commun.* **2006**, 1088.
(26) Beer, L.; Reed, R. W.; Robertson, C. M.; Oakley, R. T.; Tham, F. S.; Haddon, R. C. *Org. Lett.* **2008**, *10*, 3121.
(27) (a) Nakanishi, W.; Hayashi, S.; Toyota, S. *Chem. Commun.* **1996**, 371. (b) Nakanishi, W.; Hayashi, S.; Arai, T. *Chem. Commun.* **2002**, 2416.
(28) (a) Sharma, S.; Selvakumar, K.; Singh, V. P.; Zade, S. S.; Singh, H. B. *Phosphorus, Sulfur Silicon Relat. Elem.* **2008**, *183*, 827. (b) Kandasamy, K.; Kumar, S.; Singh, H. B.; Wolmershäuser, G. *Organometallics* **2003**, *22*, 5069. (c) Roy, D.; Patel, C.; Liebman, J. F.; Sunoj, R. B. *J. Phys. Chem. A* **2008**, *112*, 8797.

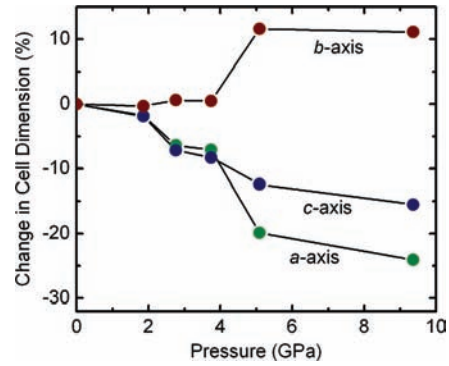

Figure 3. Changes in cell dimensions of $[\mathbf{1a}]_2$ as a function of pressure.

over the entire pressure range 0−10 GPa. The $P2_1/c$ space group is maintained, and the packing of the dimers, as viewed down the π-stacks, is similar, as can be seen in the unit cell diagram at 9.37 GPa (Figure 2). However, closer inspection of the crystal, supramolecular, and molecular architecture as a function of pressure reveals changes that are consistent with a first-order phase transition in the 4−5 GPa region. The occurrence of this phase transition is most easily demonstrated by examination of the changes in the unit cell dimensions (Table 1) with increasing pressure. Even under mild compression (pressures less than 3.74 GPa), the axial variations are not uniform. As illustrated in Figure 3, the values of *a* and *c* contract, but *b* actually increases slightly. Between 3.74 and 5.09 GPa, the divergence in the cell parameters becomes far more pronounced; the values of *a* and *c* drop rapidly, to differing degrees, while *b* rises sharply. Thereafter, and up to an applied pressure of 9.37 GPa, the cell changes become more gradual and more uniform.

The molecular and supramolecular changes associated with the phase transition can be understood with reference to Figure 4, which illustrates the evolution of the cross-bracing of the π-stacks, viewed along the *z* direction, as a function of pressure. As may be seen, very little happens below 3.7 GPa; the packing and stacking of the dimers is virtually unchanged. The value of δ_2, the plate-to-plate separation along the π-stacks, decreases slightly, as would be expected, and the inclination of the π-stacks, measured in terms of the tilt angle τ, also increases marginally, so that the molecular plates become more nearly superimposed. The dimer itself also remains much the same as at ambient pressure. The interannular Se2−Se2′ bond, the hypervalent Se2···S2 bonds and the C4−S2 bonds show small but unexceptional variations. Likewise the value of δ_1, the interplanar separation of the two halves of the dimer, remains essentially constant.

Between 3.74 and 5.09 GPa the crystal structure mutates. The large contraction in *a* and *c* and the simultaneous elongation of *b* translate into a concertina-like compression of the cross-braced framework. The plate-to-plate separation δ_2 decreases significantly, as would be expected, but there is also a change in the relative displacement or slippage of the ribbonlike arrays of dimers (Figure 5). In addition, individual ribbons appear to "buckle" under the pressure, as a result of which the planes of the two halves of the dimers separate, and δ_1 increases sharply. At the molecular level, the diselenide bond Se2−Se2′ that holds the dimers together actually lengthens, the hypervalent Se2···S2 interactions revert to values more in keeping with a covalent Se−S bond, and the C4−S2 bonds lengthen, suggesting that they are no longer best described as terminal thiones. Beyond 5.09 GPa, all structural adjustments are minor; the bonds both

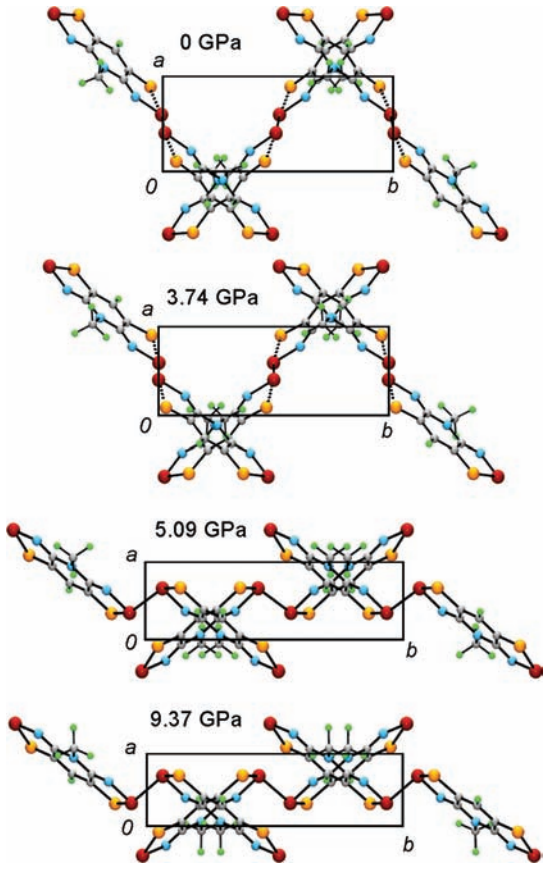

Figure 4. Cross-braced π-stacks of $[\mathbf{1a}]_2$ as a function of pressure.

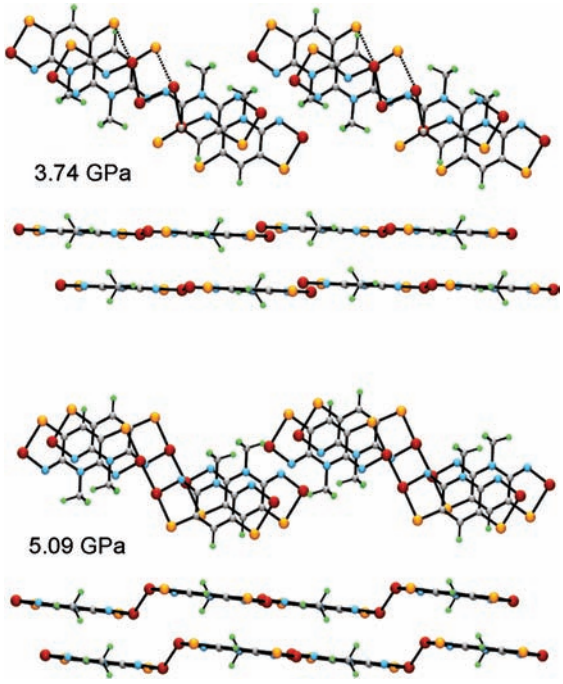

Figure 5. Slippage and buckling of ribbons of dimers, viewed from above and the side, as a function of pressure.

within and between the two halves of the dimers experience small but relatively uniform compression.

Finally, it is important to bear in mind that with compression of the lattice many close intermolecular contacts are produced, too many to allow a meaningful interpretation of all of them. It

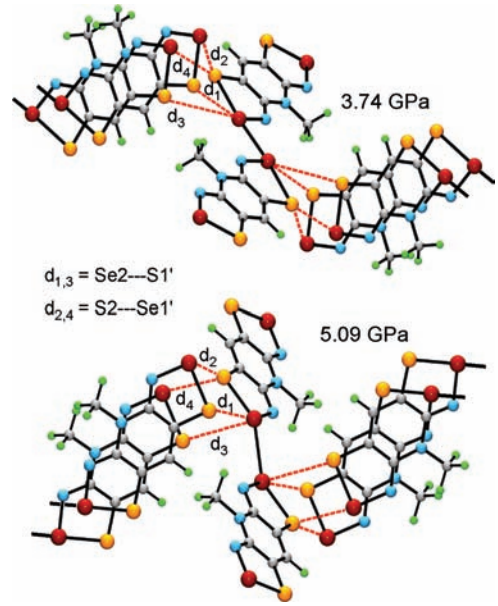

Figure 6. Intermolecular Se···S′ contacts about the diselenide core as a function of pressure.

is useful, however, to examine the changes in the interdimer Se···S′ contacts about the diselenide core as the dimer moves through the phase transition. The appearance of this unit at 3.74 and 5.09 GPa is shown in Figure 6, and values for the four contacts d_1-d_4 are listed in Table 2. Inspection of the trends in these distances shows a relatively steady decrease with increasing pressure, although in one case (d_3) the separation contracts sharply at the phase transition, whereas for another (d_2) it actually increases. That being said, even before the phase transition and most certainly afterward, the contacts d_1 and d_4 lie well inside the conventional van der Waals separation (3.7 Å) for a sulfur−selenium interaction.[22] The implications of these close contacts on the electronic structure of the dimer are discussed below.

Conductivity Measurements. In previous work we determined the room temperature conductivity of $[\mathbf{1a}]_2$ to be on the order of 10^{-6} S cm^{-1} at ambient pressure and the thermal activation energy E_{act} over the temperature range $T = 300-360$ K to be near 0.32 eV.[15] We also explored the variation in conductivity and activation energy with pressure by means of a cubic anvil press and established that the conductivity could be increased by 5−6 orders of magnitude by the application of 5 GPa pressure.[15] At the same time the value of E_{act} was reduced to near 0.03 eV. To gain a clearer picture of the response of $[\mathbf{1a}]_2$ to pressure, we have performed two new series of measurements. The first series represents an extension of the earlier cubic anvil press experiments, which were confined to an upper pressure limit of 5 GPa. Using a Walker module we have been able to extend the pressure limit to 9 GPa and thereby secure information on the dependence of the activation energy at ambient temperatures for pressures near and above the phase transition identified in the crystallographic work. The variation in the E_{act} with pressure over the range $T = 300-360$ K using these two techniques is illustrated in Figure 7.

The trends in E_{act} with increasing pressure obtained from the two techniques are convincingly consistent, especially when one considers that E_{act} is a quantity derived from slopes of conductivity versus inverse temperature plots. However, the E_{act} values from the Walker module experiments appear to be shifted

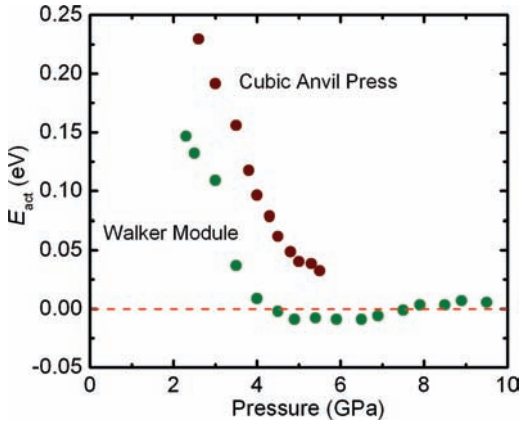

Figure 7. Pressure dependence of the activation energy, E_{act}, for conductivity of $[\mathbf{1a}]_2$ over the range $T = 300-360$ K.

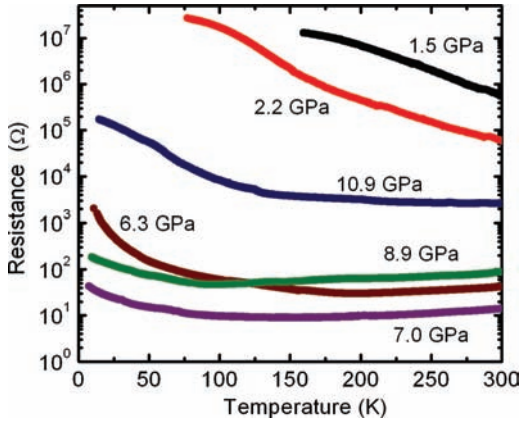

Figure 8. Temperature dependence of resistance of $[\mathbf{1a}]_2$ in the range $T = 4-300$ K at different pressures.

to lower pressure compared with the cubic anvil values. This may result from the differences in pressure calibration in the two devices as well as the differences in hydrostaticity of the pressure medium used in each device (pyrophyllite versus MgO). Pyrophyllite is softer than MgO, which may partially explain the delayed response of the cubic press results, that is, the slight shift to higher pressure. Nonetheless, the data from both experiments point to a rapid decrease in activation energy with applied pressure, to a value of zero or near to it, in the region of 4−9.5 GPa. Indeed the Walker module data affords slightly negative values for E_{act} over the range of 5−7 GPa, a result which can be interpreted in terms of the formation of a weakly metallic state. The variations in E_{act} thereafter, including the slight increase at elevated pressures, are less than the value of kT at these temperatures and may simply reflect the way the value of E_{act} was derived.

To explore the behavior of $[\mathbf{1a}]_2$ under pressure at low temperatures, we turned to the use of a diamond anvil cell. These measurements did not afford conductivity values, as we were unable to obtain accurate measurements of sample dimensions, but the temperature dependence of the raw resistance data provides a clear indication of the dependence of the activation energy E_{act} on applied pressure. The results of these experiments, which are illustrated in Figure 8, complement those obtained from the high temperature measurements. At low pressures (1.5 GPa), the resistance is high and decreases with temperature, as expected for a semiconductor. With increasing pressure the resistance decreases less rapidly with temperature, indicating a

Table 3. Calculated Metrics[a] and Frontier Orbital Energies[b] for $[\mathbf{1a}]_2$ at Different Pressures

	Pressure, GPa			
	0.70	2.87	5.27	9.00
a, Å	5.252	4.555	3.902	3.765
b, Å	12.157	12.724	13.895	13.877
c, Å	15.236	13.836	13.306	12.783
β, deg	98.358	89.157	86.788	86.384
V, Å^3	962.50	801.84	720.27	666.59
Se2−Se2′, Å	2.512	2.459	2.482	2.496
Se2···S2, Å	2.752	2.702	2.464	2.295
δ_1, Å	0.310	0.283	1.370	1.623
δ_2, Å	3.703	3.229	3.060	2.958
ϕ, deg	169.2	166.6	155.3	146.7
ε_{LUMO}, eV	−3.3059	−3.2931	−3.3712	−3.4866
ε_{HOMO}, eV	−5.0676	−5.0478	−4.3231	−4.0619

[a] The unconventional cell settings (with $\beta < 90°$) at higher pressure were used so as to allow a direct comparison across all of the structures. [b] Single point B3LYP/6-31G(d,p) eigenvalues.

lowering of the activation energy. The measurements carried out over the pressure range 6.3−8.9 GPa reveal a regime of weakly metallic behavior for temperatures above 200 K. However, cooling below this temperature (at 6.3 GPa) or below 100 K at 8.9 GPa affords a region where the conductance (1/R) returns to being activated. It should also be noted that the resistance in the weakly metallic zone reaches a minimum at 7.0 GPa. Thereafter, sample resistance begins to increase with increasing pressure. From these results we conclude that at moderate temperatures (150−350 K) and pressures (5−9 GPa) $[\mathbf{1a}]_2$ behaves as a weak metal, but at low temperatures and more extreme pressures it reverts to a semi-metallic state. The interpretation of these features in terms of the electronic structure of the material is developed below.

Band Structure Calculations. The room temperature electronic structure of $[\mathbf{1a}]_2$ has been probed by a series of ab initio calculations using the VASP package. Using the experimental structures at various pressures as starting points, complete optimizations of both geometry and pressure were performed. The numerical results of calculations at four representative pressures are summarized in Table 3, which lists the unit cell parameters and pertinent internal structural parameters. These may be compared with the corresponding experimental values listed in Table 2. A visual comparison of the calculated molecular structure of the dimer itself at the four pressures is shown in Figure 9. Full details of the calculated molecular and solid-state geometries (in CIF format) are available in Supporting Information.

Given the dimensions of the problem, the calculated structural parameters as a function of pressure track the observed values remarkably accurately, at both the molecular and solid-state levels. The direction and magnitude of the unit cell changes parallel those seen experimentally, both qualitatively and quantitatively. Thus, the values of a and c contract sharply through the phase transition, while b elongates, to afford the concertina-like compression of the slipped π-stacks. The decrease in the interplanar separation of dimers along the π-stacks (δ_2) also follows closely the trends seen experimentally. Likewise, at a molecular level, the calculations reproduce the major changes in the dimeric unit of $[\mathbf{1a}]_2$ as a function of pressure. As can be seen in Figure 9, the increase in the value of δ_1, the separation of the planes of the two halves of the dimer, which heralds the phase transition, is well replicated, as is the closure of the hypervalent Se2···S2 contact to a distance more in keeping with a covalent Se−S bond.

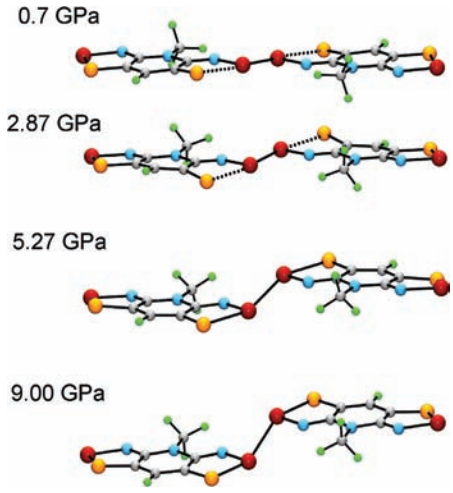

Figure 9. Calculated molecular structure of $[\mathbf{1a}]_2$ at different pressures.

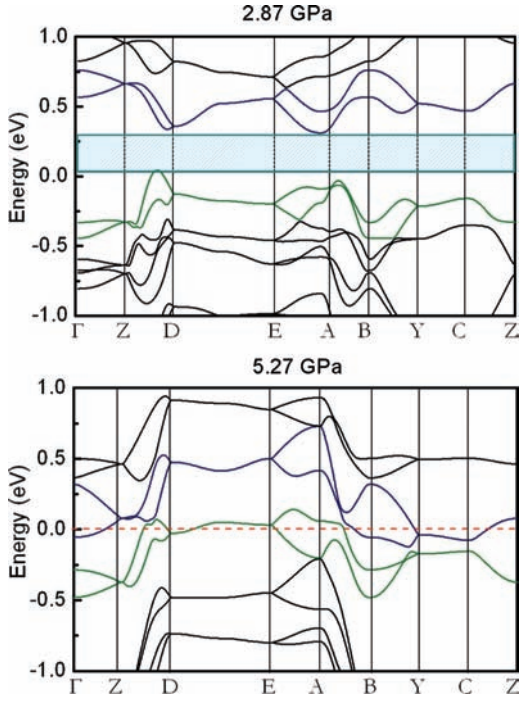

Figure 10. Crystal orbital energy dispersion of $[\mathbf{1a}]_2$ at calculated pressures of 2.87 and 5.27 GPa. Crystal orbitals for the valence (green) and conduction (blue) bands are highlighted. The band gap (at 2.87 GPa) is hatched.

On the basis of the correspondence of the calculated and observed geometries, we have examined the band electronic structure of $[\mathbf{1a}]_2$ as a function of pressure, using the four calculated geometries as reference points. As indicated at the outset, the intent of this work has been to determine the cause of the metallization of this material, in particular whether it could be attributed to the closure of an electronic energy band gap. That this is indeed the case is demonstrated in Figure 10, which shows crystal orbital dispersion diagrams at pressures just below (2.87 GPa) and just above (5.27 GPa) the phase transition.[29] As may be seen, at low pressures, that is, below 3 GPa, there is a well-defined energy gap, E_g, between the valence and conduction bands. At 2.87 GPa, E_g is 0.34 eV, a value that is

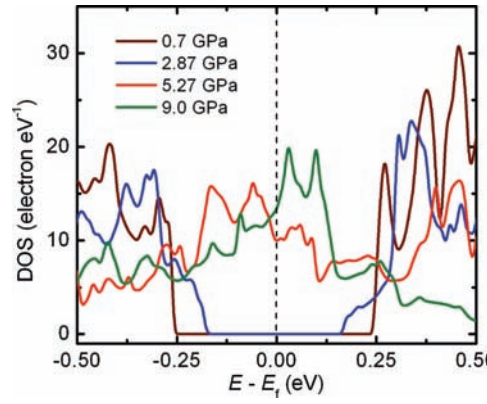

Figure 11. Density of states (DOS) of $[\mathbf{1a}]_2$ as a function of pressure.

less than that found at 0.7 GPa ($E_g = 0.50$ eV)[30] and consistent with improved but still activated conductivity. This decrease in band gap does not suggest the likelihood of imminent band gap closure with increasing pressure. At 2.87 GPa, for example, the valence and conduction bands are both on the order of 0.5 eV in width, and considerable band broadening would be required to afford coalescence. Such a conclusion does not, however, take into account the phase transition and concomitant electronic changes that take place in the region of 4−5 GPa. Thus, as may be seen in the dispersion energy plots at 5.27 GPa, compression through the phase transition to 5.27 GPa causes the entire valence band to rise and the conduction band to drop in energy. This mutual approach, coupled with band spreading, gives rise to valence/conduction band overlap and complete closure of the band gap. Beyond this point, up to 9.00 GPa, additional compression of the transformed structure leads to increasing interpenetration of the valence and conduction bands. It is important to note that the electronic structure of the high pressure material is more semi-metallic than metallic, as the overlap of the two bands is largely indirect. Density of states (DOS) calculations (Figure 11) also suggest that closure of the band gap at 5.27 GPa and even 9.00 GPa does not lead to a large DOS at the Fermi level E_f.

Discussion

The high pressure crystallographic studies on $[\mathbf{1a}]_2$ provide a clear view of the molecular and solid-state structural changes associated with the onset of a metallic state in the 4−5 GPa region. The band structure calculations replicate these changes as a function of pressure remarkably well and predict the closure of the band gap. However, the results indicate that while coalescence of the valence and conduction bands can be partly attributed to band broadening arising from enhanced intermolecular interactions, it also appears to involve a mutual approach of the valence and conduction bands at the phase transition. This led us to suspect that the buckling of the molecular structure of $[\mathbf{1a}]_2$ might be giving rise to changes in its electronic structure. To explore this possibility we performed a series of DFT calculations, at the B3LYP/6-31G(d,p) level, on the molecular electronic structure of $[\mathbf{1a}]_2$ as a function of pressure. Our intent was to track changes in frontier molecular orbital energies of the dimer, that is, the DFT eigenvalues ε_{HOMO} and ε_{LUMO}, using atomic coordinates obtained from the pressure and

(29) Crystal orbital dispersion diagrams at 0.70 and 9.00 GPa are available as Supporting Information.

(30) This value may be compared with that (0.31 eV) obtained previously[15] from single point LMTO calculations based on the ambient pressure crystal structure.

Chart 2

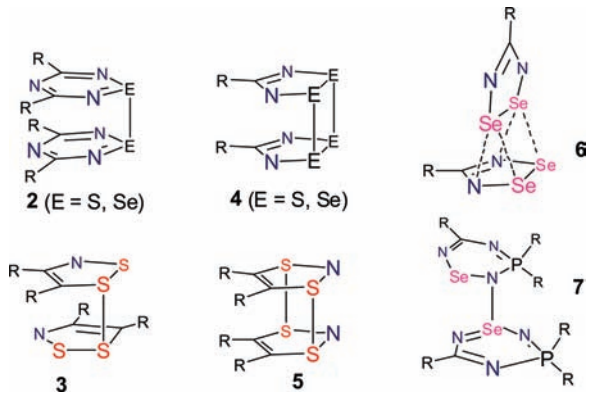

geometry optimized VASP calculations. The results, summarized in Table 3, indicate little change in the frontier eigenvalues between 0.70 and 2.87 GPa. However, after the phase transition, at 5.27 and 9.00 GPa, the HOMO rises sharply, causing a significant decrease in the HOMO−LUMO gap and heralding a significant electronic reorganization of the dimer itself. It would thus appear that the metallization of $[\mathbf{1a}]_2$ arises as much from intramolecular effects, which give rise to band shifting, as from increased intermolecular interactions, which cause band spreading.

Before addressing the reason for the closure of the HOMO−LUMO gap of $[\mathbf{1a}]_2$ with pressure, it is instructive to review how selenazyl (−Se−N−) and thiazyl (−S−N−) π-radicals can associate. For both families the most common mode of dimerization involves the direct pairing of π-electrons (Chart 2). The orientation of the two radicals is usually (but not always) cofacial and may involve the interaction of one heavy (S/Se) atom (**2**, **3**)[31] or two (**4**, **5**),[32,33] although for selenium-centered radicals other more unusual modes of association (**6**, **7**)[34,35] have been observed. In all cases, however, the formation of the dimer involves no change in the electronic configuration as the two radicals approach. The weak interdimer bond is reasonably described in terms of the overlap of two π-SOMOs, as may be seen in Figure 12, which illustrates the association of a monocyclic 7π-electron 1,2,3-thiaselenazolyl radical [H_2C_2SSeN] along an axis through both selenium atoms and perpendicular to the planes of the two radicals.

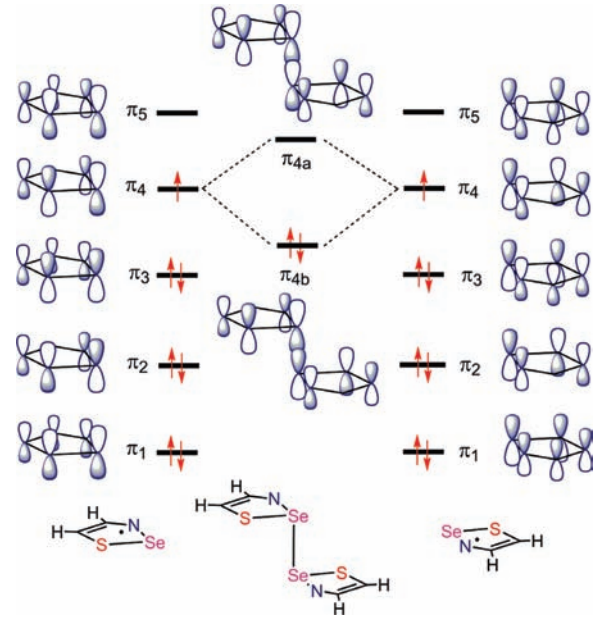

Figure 12. Overlap of SOMOs of two 1,2,3-thiaselenazolyl radicals to form a π-dimer.

In hypervalent σ-dimers such as $[\mathbf{1a}]_2$, radical association cannot be envisaged in terms of the overlap of π-SOMOs. Instead a change in electronic configuration of the radicals is required for the dimerization to occur; essentially a pair of electrons from the π-system must be transferred into the σ-system in order to generate the electron-rich σ-bonds. In valence bond terms this transfer can be understood by inspection of the Lewis representations of **1** and $[\mathbf{1}]_2$ shown in Chart 1; there are 17 π-electrons on each radical, or a total of 34 valence π-electrons on two, whereas in the hypervalent dimer there are only 32 valence π-electrons. The consequences of this difference are most conveniently developed within a molecular orbital context, and to this end we illustrate in Figure 13 a correlation diagram showing the frontier molecular orbitals of the π- and σ-dimers[36] of a simple, monocyclic 7π-thiaselenazolyl, the basic building block of radical **1**. As may be seen, in the π-dimer of this model, one of the π_4 levels (from Figure 12) is occupied, and there is also a pair of occupied bonding S−Se σ-orbitals (σ_1, σ_2), as well as their unoccupied antibonding counterparts (σ_3, σ_4). By contrast, in the σ-dimer both of the π_4-orbitals are virtual, and the released electron pair now occupies σ_3, thereby creating the hypervalent 4c-6e σ-manifold.

The energetic and structural consequences of the σ/π configurational change are profound. Interconversion of the π- and σ-dimers, a process that can be driven by varying the "plate

(31) (a) Hayes, P. J.; Oakley, R. T.; Cordes, A. W.; Pennington, W. T. *J. Am. Chem. Soc.* **1985**, *107*, 1346. (b) Oakley, R. T.; Reed, R. W.; Cordes, A. W.; Craig, S. L.; Graham, S. B. *J. Am. Chem. Soc.* **1987**, *109*, 7745. (c) Barclay, T. M.; Beer, L.; Cordes, A. W.; Oakley, R. T.; Preuss, K. E.; Taylor, N. J.; Reed, R. W. *Chem. Commun.* **1999**, 531.

(32) (a) Cordes, A. W.; Haddon, R. C.; Oakley, R. T.; Schneemeyer, L. F.; Waszczak, J. V.; Young, K. M.; Zimmerman, N. M. *J. Am. Chem. Soc.* **1991**, *113*, 582. (b) Andrews, M. P.; et al. *J. Am. Chem. Soc.* **1991**, *113*, 3559. (c) Cordes, A. W.; Haddon, R. C.; Hicks, R. G.; Oakley, R. T.; Palstra, T. T. M.; Schneemeyer, L. F.; Waszczak, J. V. *J. Am. Chem. Soc.* **1992**, *114*, 1729. (d) Britten, J. F.; Clements, O. P.; Cordes, A. W.; Haddon, R. C.; Oakley, R. T.; Richardson, J. F. *Inorg. Chem.* **2001**, *40*, 6820. (e) Beer, L.; Cordes, A. W.; Myles, D. J. T.; Oakley, R. T.; Taylor, N. J. *CrystEngChem* **2000**, *2*, 109. (g) Bryan, C. D.; Cordes, A. W.; Oakley, R. T.; Spence, R. E. v. H. *Acta Crystallogr. C* **1995**, *51*, 2402. (h) Cordes, A. W.; Glarum, S. H.; Haddon, R. C.; Hallford, R.; Hicks, R. G.; Kennepohl, D. K.; Oakley, R. T.; Palstra, T. T. M.; Scott, S. R. *J. Chem. Soc., Chem. Commun.* **1992**, 1265. (i) Parvez, M.; Boeré, R. T. *Acta Crystallogr. C* **1995**, *51*, 2118.

(33) (a) Vegas, A.; Pérez-Salazar, A.; Banister, A. J.; Hey, R. G. *J. Chem. Soc., Dalton Trans.* **1980**, 1812. (b) Banister, A. J.; Rawson, J. M. *Adv. Heterocycl. Chem.* **1995**, *62*, 137. (c) Awere, E. G.; Burford, N.; Haddon, R. C.; Parsons, S.; Passmore, J.; Waszczak, J. V.; White, P. S. *Inorg. Chem.* **1990**, *29*, 4821. (d) Awere, E. G.; Burford, N.; Mailer, C.; Passmore, J.; Schriver, M. J.; White, P. S.; Banister, A. J.; Oberhammer, M.; Sutcliffe, L. H. *J. Chem. Soc., Chem. Commun.* **1987**, 66. (e) Brusso, J. L.; Clements, O. P.; Haddon, R. C.; Itkis, M. E.; Leitch, A. A.; Oakley, R. T.; Reed, R. W.; Richardson, J. F. *J. Am. Chem. Soc.* **2004**, *126*, 14692. (f) Alberola, A.; Clements, O. P.; Collis, R. J.; Cubbitt, L.; Grant, C. M.; Less, R. J.; Oakley, R. T.; Rawson, J. M.; Reed, R. W.; Robertson, C. M. *Cryst. Growth Des.* **2008**, *8*, 155.

(34) Bestari, K.; Cordes, A. W.; Oakley, R. T.; Young, K. M. *J. Am. Chem. Soc.* **1990**, *112*, 2249.

(35) Feeder, N.; Less, R. J.; Rawson, J. M.; Oliete, P.; Palacio, F. *Chem. Commun.* **2000**, 2449.

(36) The ordering of levels in Figures 12 and 13 is based on the results of B3LYP/6-31G(d,p) calculations. The terms σ and π are used for convenience; the correlation lines in Figure 13 connect orbitals according to their inversion symmetry.

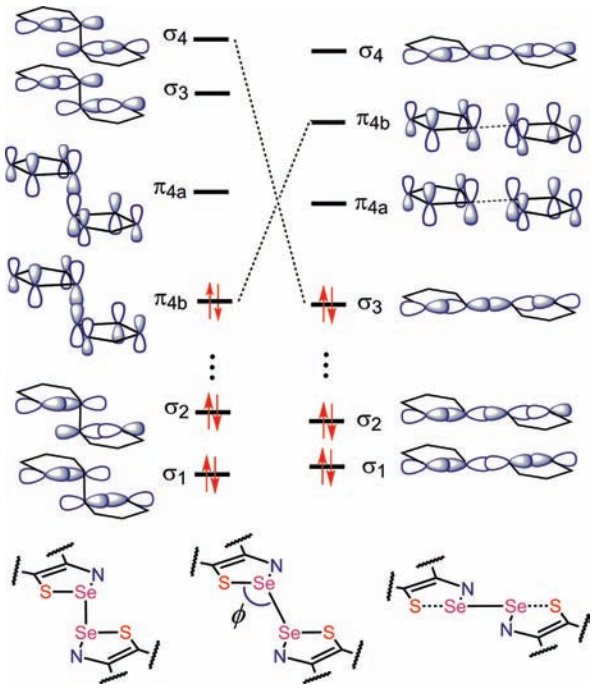

Figure 13. Frontier molecular orbitals of the π- and σ-dimers of a 1,2,3-thiaselenazolyl radical.

buckling" angle ϕ from 90° to 180°, requires the mixing in of high-lying virtual orbitals, as shown by the (dashed) correlation lines in Figure 13. This avoided crossing is expected to give rise to an energy barrier between the two dimers that is compensated by the external (PV) work done by the applied pressure. To explore the magnitude of this barrier, and the location of the transition state (ϕ value), we carried out a series of B3LYP/6-31G(d,p) calculations on $[\mathbf{1a}]_2$. The results are shown in Figure 14, in the form of plots of the total energy of the dimer, its HOMO and LUMO eigenvalues[37] and the intra-annular S−Se and interannular Se−Se distances as a function of plate buckling. As may be seen, these energetic and structural parameters all undergo abrupt changes near $\phi = 140°$ that herald the onset of the configurational change. Thus, the total electronic energy surface from $\phi = 90°$ to 180° may be viewed as an overlay of a shallow potential energy well for the distortion of the π-dimer with a deeper well associated with buckling of the σ-dimer, the two curves intersecting near $\phi = 140°$. Likewise the sharp discontinuity in the frontier orbital energies and simultaneous collapse of the HOMO−LUMO gap are symptomatic of the major change in orbital makeup accompanying the configurational crossover. The reversal in the phase of the frontier orbital wave functions predicted by the molecular calculations is evident in the electron band dispersion along Z → D (Figure 10). Thus, in the insulating state (2.87 GPa), the conduction band energies close to the Fermi level decrease, while after band closure (5.07 GPa) these bands rise sharply. This facilitates overlap between dimers, resulting in a bulk conductor. Finally, from a structural perspective, the simultaneous contraction in the interannular Se−Se bond and lengthening of the intra-annular S−Se bond with decrease in ϕ serve as

(37) There are slight differences in the ordering of the B3LYP/6-31G(d,p) π- and σ-levels of $[\mathbf{1a}]_2$ relative to those illustrated for the model dimers in Figures 12 and 13. At $\phi = 180°$, for example, the σ_3 Se−Se bonding orbital is the HOMO-1, and the HOMO is of π-symmetry.

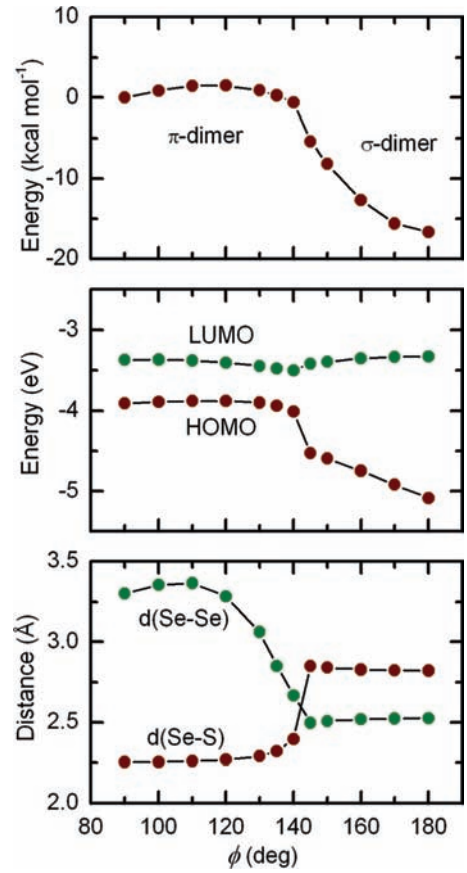

Figure 14. Total electronic energy of $[\mathbf{1a}]_2$ (top), ε_{HOMO} and ε_{LUMO} values (center), and the intra-annular S−Se and interannular Se−Se distances (bottom) as a function of ϕ.

persuasive signatures of the conversion of a π-dimer into a hypervalent σ-dimer.

In the light of these molecule-based calculations, the nature of the phase transition in $[\mathbf{1a}]_2$ and its consequences on transport properties can be readily understood. At a structural level, the planar σ-dimer ($\phi = 180°$) is predicted to be the favored geometry at ambient pressure. Initially, the application of pressure is expected to have little effect. Buckling of the 4c-6e σ-dimer structure is not only energetically disfavored, but if it were to occur, it would afford little potential gain in terms of structural compression. That is to say, for small changes in ϕ the calculated (and experimental) values of Se−Se and S···Se distances remain relatively constant. As a result, for pressures up to 4−5 GPa, the molecular structure of $[\mathbf{1a}]_2$ remains essentially unchanged; contraction of the unit cell arises primarily from a shortening of intermolecular contacts rather than chemical bonds. Pressures above 5 GPa, however, are sufficient to induce a compression in the linear S···Se−Se···S sequence. Such a process requires a buckling of the dimer as the hypervalent σ-dimer configuration evolves into a more conventional π-dimer configuration. Compression is maximized, that is, the overall length of the approximately linear 4-atom sequence reaches a minimum value, near $\phi = 140°$. Continued buckling beyond this point does not occur, as it would lead to a rapid increase in d(Se−Se), and an expansion in both molecular and cell volume.

We therefore conclude that it is the *partial* buckling of $[\mathbf{1a}]_2$ (to $\phi \approx 140°$) rather than its complete transformation into a superimposed ($\phi = 90°$) π-dimer that provides the most *compact*

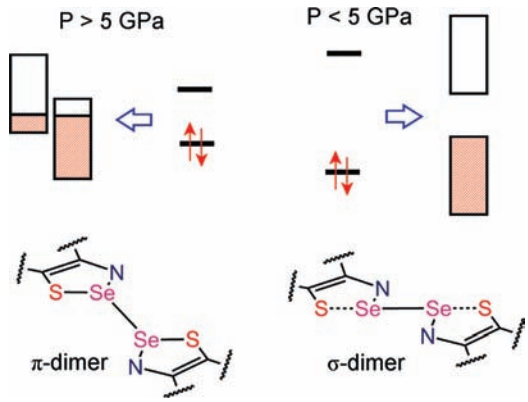

Figure 15. Summary of structural and electronic changes in $[\mathbf{1a}]_2$ under pressure.

molecular structure. From an electronic perspective, the molecular orbital reorganization required to allow the structural change leads to a marked decrease in the HOMO−LUMO gap, as a result of which valence-conduction band overlap can be achieved without the need for major band broadening (Figure 15). In essence, metallization arises as much from the response of the molecule to pressure as it does to the more general effects of enhanced intermolecular interactions.

Summary and Conclusions

The use of physical pressure to increase the conductivity of closed shell molecular compounds is traditionally based on the premise that the chemical bonds within the molecular building blocks are not affected significantly by the application of external pressure. Within the confines of this assumption and, in addition, in the absence of irreversible molecular decomposition, enhancements in conductivity may then be reasonably attributed to the closure of the valence/conduction band gap as a result of increased intermolecular interactions and consequent band broadening.

The present work reveals a new dimension in study of the structure and properties of molecular solids under pressure. It provides a unique example of a reversible structural rearrangement of a molecule driven by pressure. The molecule in question is the radical dimer $[\mathbf{1a}]_2$, formed by the association of the bisthiaselenazolyl radical **1a**. In contrast to most other heavy atom (S, Se) based π-radicals, which associate through overlap of their π-SOMOs, **1a** dimerizes laterally by means of a hypervalent 4c-6e S···Se−Se···S σ-bond. With the application of pressure, however, this linear arrangement buckles to afford a structure that is best described as a highly distorted π-dimer. While the conversion of a σ-dimer to a π-dimer is, in itself, a novel result, what makes the process truly remarkable is the fact that the σ- to π-dimer crossover leads, as a result of an avoided crossing, to a sudden closure in the HOMO−LUMO gap. As a result, even a moderate degree of broadening of the associated valence and conduction bands gives rise to complete closure of the band gap and the formation of a material with a metallic ground state. In a very real sense, the σ- to π-dimer switch transforms $[\mathbf{1a}]_2$ from a molecule into a metal.

Much work remains to be done with $[\mathbf{1a}]_2$. For example, preliminary decompression experiments on $[\mathbf{1a}]_2$ indicate a considerable lag in the recovery of the original structure, a process that may be slowed at reduced temperatures. Will it be possible, therefore, to depressurize a metallic system at low temperatures and trap the dimer in a metastable metallic state at ambient pressure? Apart from $[\mathbf{1a}]_2$, there are already several other recently reported radicals of this type, some based on sulfur, and others on selenium. Similar or even quite unrelated pressure related rearrangements may occur for these systems, and these may also give rise to dramatic variations in conductive and/or magnetic properties.

Experimental and Computational Methods

Sample Preparation. Microcrystalline samples of $[\mathbf{1a}]_2$ suitable for powder diffraction work were generated by reduction of the salt [**1a**][OTf] (OTf = trifluoromethanesulfonate) with decamethylferrocene. Details of the procedure and the preparation of [**1a**][OTf] are described elsewhere.[15]

Crystallography. High pressure diffraction experiments on $[\mathbf{1a}]_2$ were performed at BLX10U, SPring-8, using synchrotron radiation (λ = 0.51446 Å) and a powdered sample mounted in a diamond anvil cell, with helium as the pressure transmitting medium.[38] The diffraction data were collected at room temperature and as a function of *increasing* pressure. A total of five data sets (from 0−9.37 GPa) were indexed and the cell parameters refined using DASH 3.01.[39] The structures were solved in DASH starting from a model radical **1a** derived from a fully optimized UB3LYP/6-311G(d,p) calculation. During the initial Rietveld[40] refinement in DASH a rigid-body constraint was maintained, but the sulfur and selenium positions were later released to optimize within the plane of the molecule. At this point the space group settings were adjusted so as to allow a direct comparison of all the high pressure cell parameters with those published for the ambient pressure crystal structure. These settings and the atomic coordinates were then taken into GSAS[41] for a final Rietveld refinement. Data from $2\theta = 3-20°$ were refined with fixed atomic positions and isotropic thermal parameters with an assigned value of 0.025.

Conductivity Measurements. High pressure−temperature conductivity experiments on $[\mathbf{1a}]_2$ were carried out using two different types of large volume presses and with a diamond anvil cell. In the 1000 ton cubic anvil press[42] using pyrophyllite ($Al_4Si_8O_{20}(OH)_4$) as the pressure transmitting medium and a 500 ton multi-anvil press equipped with a Walker module[43] using MgO as the pressure transmitting medium, sample pressure was determined from previous calibrations[42,44] of the applied hydraulic load against pressures of structure transformations in standards at room temperature (Bi I−II at 2.46 GPa and III−VII at 7.7 GPa, Tl I−III at 3.70 GPa, and ZnTe I−I′ at 6.6 GPa and I′−II at 8.9 GPa). The pressure cell design[45] was modified to include a Nb furnace, and Pt disk electrodes contacted the precompacted, powder samples contained in a boron nitride ($\sigma_{BN} = 10^{-11}$ S cm^{-1}) cup. Contacts to the Pt disks were made with Re/W (97%/3%) wires. Four wire AC (Solartron 1260 impedance analyzer) resistance measurements were made at a frequency of either 1 or 100 kHz. The contiguous disk-shaped sample was extracted from the recovered pressure cell, and the sample geometry was measured to convert resistance to conductivity. Infrared analysis of the sample recovered from the Walker module experiments confirmed its integrity. There was no

(38) Initial powder diffraction measurements without a pressure transmission medium were made on the HXMA (high energy X-ray materials analysis) beamline of the Canadian Light Source. A structural phase transition was observed at 4−5 GPa, but the quality of the data was not good enough for structural refinement.
(39) David, W. I. F.; Shankland, K.; van de Streek, J.; Pidcock, E.; Motherwell, W. D. S.; Cole, J. C. *J. Appl. Crystallogr.* **2006**, *39*, 910.
(40) Rietveld, H. M. *J. Appl. Crystallogr.* **1969**, *2*, 65.
(41) Larson, A. C.; Von Dreele, R. B. Report No. LA-UR-86-748; Los Alamos National Laboratory: Los Alamos, NM, 1987.
(42) Secco, R. A. *Can. J. Phys.* **1995**, *73*, 287.
(43) Walker, D.; Carpenter, M. A.; Hitch, C. M. *Am. Mineral.* **1990**, *76*, 1020.
(44) Secco, R. A.; Liu, H.; Imanaka, N.; Adachi, G. *J. Mater. Sci. Lett.* **2001**, *20*, 1339.
(45) Wang, D.; Mookherjee, M.; Xu, Y.; Karato, S. *Nature* **2006**, *443*, 977.

evidence, by comparison with the infrared spectrum of an unpressurized sample,[15] of any deterioration after the excursion to 9 GPa.

In the diamond anvil cell measurements the evolution of electrical resistance with pressure was investigated by the four-probe technique. Pressure was generated by a pair of diamonds with a 600 μm diameter culet. A sample hole of 300 μm diameter was drilled in the gasket after its thickness was reduced from 250 to 30 μm by preindentation. It was then covered with a thin layer of cubic boron nitride BN for electrical insulation between the gasket and the electrodes. Gold wire of 18 μm diameter was used as electrode leads. The pressure was determined by the ruby fluorescence method at room temperature before and after each cooling cycle. A rough estimate of the conductivity from the resistance measurement was consistent with the bulk measurement from the cubic anvil cell.

Solid-State Electronic Structure Calculations. All calculations were performed with the electronic code VASP (Vienna Ab initio Structure Package)[46] employing projector augment wave potentials[47] (PAW) to replace the core orbitals of all elements except H. The Perdew−Burke−Ernzerhof exchange and correlation functionals[48] within the generalized gradient approximation were used. The wave functions were expanded in plane wave basis sets. A grid of $4 \times 2 \times 2$ *k*-points was used in the SCF and geometry optimization calculations. A denser $16 \times 4 \times 4$ *k*-point set was used for the calculation of the electron density of states.

Molecular Electronic Structure Calculations. All DFT calculations were performed using the Gaussian 09W suite of programs.[49] For the studies of plate buckling the B3LYP hybrid functional and polarized, split-valence basis sets with double-ζ (6-31G(d,p)) and triple-ζ (6-311G(d,p)) functions were employed. Geometry optimization as a function of the buckling angle ϕ was invoked with the restriction that, for both the model 1,2,3-thiaselenazolyl radical dimer and $[\mathbf{1a}]_2$, the geometry of each half of the dimeric unit was held planar and the methyl group of $[\mathbf{1a}]_2$ was held rigid. Coplanarity of the S···Se−Se···S sequence was also enforced. It should be noted that in the actual structure of $[\mathbf{1a}]_2$ this 4-atom unit is not rigorously coplanar. The departure of the experimental values of ϕ from 180° in the ambient and low pressure (<5 GPa) crystal structures can be largely attributed to this effect.

Acknowledgment. We thank the Natural Sciences and Engineering Research Council of Canada (NSERCC) and the NSF and MOST of China for financial support. We also thank the NSERCC for a Canada Graduate Scholarship to A.A.L., the Government of Canada for a Tier I Canada Research Chair to J.S.T., the Canada Council for a Killam Research Fellowship to R.T.O., and the Japan Synchrotron Radiation Research Institute (JASRI) for beam time. Synchrotron work at the Canadian Light Source was made possible by support from the NSERCC, NRC, CIHR, and the University of Saskatchewan.

Supporting Information Available: Complete authorship for refs 32b and 49. VASP calculated structure of $[\mathbf{1a}]_2$ and band dispersion diagrams as a function of pressure. Observed and calculated powder diffraction patterns for $[\mathbf{1a}]_2$ as a function of pressure. Details of crystallographic data collection and structure refinement, tables of atomic coordinates, bond distances and angles, and isotropic thermal parameters in CIF format. Details of dimer buckling calculations. This material is available free of charge via the Internet at http://pubs.acs.org.

JA100216C

(46) (a) Kresse, G.; Hafner, J. *Phys. Rev.* **1993**, *47B*, 558. (b) Kresse, G.; Furthmüller, J. *Phys. Rev.* **1996**, *54B*, 11169.
(47) (a) Blöchl, P. E. *Phys. Rev.* **1994**, *50B*, 17953. (b) Kresse, G.; Joubert, J. *Phys. Rev.* **1999**, *59B*, 1758.
(48) Perdew, J. P.; Burke, K.; Ernzerhof, M. *Phys. Rev. Lett.* **1996**, *77*, 3865.
(49) Frisch, M. J. et al. *Gaussian 09, Revision A.02*; Gaussian, Inc.: Wallingford, CT, 2009.